

The far-infrared–radio correlation in MS0451-03

S. M. Randriamampandry,^{1,2★} S. M. Crawford,¹ C. M. Cress,^{2,3} K. M. Hess,⁴
M. Vaccari,² E. M. Wilcots,⁵ M. A. Bershadsky⁵ and G. D. Wirth⁶

¹South African Astronomical Observatory, PO Box 9, Observatory 7935, South Africa

²Department of Physics, University of the Western Cape, Private Bag X17, Bellville 7535, South Africa

³Centre for High Performance Computing, 15 Lower Hope Street, Rosebank, Cape Town 7700, South Africa

⁴Astrophysics, Cosmology and Gravity Centre (ACGC), Astronomy Department, University of Cape Town, Private Bag X3, 7701 Rondebosch, South Africa

⁵University of Wisconsin-Madison, 475 North Charter Street Madison, WI 53706, USA

⁶W.M. Keck Observatory, 65-1120 Mamalahoa Highway, Kamuela HI 96743, USA

Accepted 2014 November 13. Received 2014 November 12; in original form 2013 September 16

ABSTRACT

We present a multiwavelength analysis of star-forming galaxies in the massive cluster MS0451.6-0305 at $z \sim 0.54$ to shed new light on the evolution of the far-infrared–radio relationship in distant rich clusters. We have derived total infrared luminosities for a spectroscopically confirmed sample of cluster and field galaxies through an empirical relation based on *Spitzer* Multiband Imaging Photometer for *Spitzer* 24 μm photometry. The radio flux densities were measured from deep Very Large Array 1.4 GHz radio continuum observations. We find the ratio of far-infrared to radio luminosity for galaxies in an intermediate-redshift cluster to be $q_{\text{FIR}} = 1.80 \pm 0.15$ with a dispersion of 0.53. Due to the large intrinsic dispersion, we do not find any observable change in this value with either redshift or environment. However, a higher percentage of galaxies in this cluster show an excess in their radio fluxes when compared to low-redshift clusters (27^{+23}_{-13} per cent to 11 per cent), suggestive of a cluster enhancement of radio-excess sources at this earlier epoch. In addition, the far-infrared–radio relationship for blue galaxies, where $q_{\text{FIR}} = 2.01 \pm 0.14$ with a dispersion of 0.35, is consistent with the predicted value from the field relationship, although these results are based on a sample from a single cluster.

Key words: cosmic rays–galaxies: clusters: general–galaxies: photometry–radio continuum: galaxies.

1 INTRODUCTION

Radio continuum emission from normal star-forming galaxies can be a powerful tracer of recent star formation activity (Condon 1992). The radio luminosities at 1.4 GHz are tightly correlated with the far-infrared (IR) luminosities for various galaxy types (e.g. van der Kruit 1971; Helou, Soifer & Rowan-Robinson 1985; Condon, Anderson & Helou 1991) over a wide range of redshift (e.g. Garrett 2002; Appleton et al. 2004; Jarvis et al. 2010; Ivison et al. 2010a; Sargent et al. 2010a).

The correlation is believed to be driven by the internal star formation rate. Radio emissions from these galaxies are predominantly produced from the synchrotron emission of cosmic ray electrons accelerated in supernova shocks. The IR emission is due to ultraviolet light from young massive stars that is absorbed and re-radiated by dust (Condon 1992). However, it is still unclear what maintains this

strong correlation seen over such a wide range of galaxies (Murphy 2009).

The relationship shows lower far-IR to radio luminosity ratios in galaxy clusters than that found in the field (Andersen & Owen 1995; Reddy & Yun 2004) with much of the variation coming from a subset of objects with large deviations from the relationship (Miller & Owen 2001). A number of different processes drive the evolution of galaxies in clusters such as gravitational interactions and ram pressure (see e.g. Boselli & Gavazzi 2006, for a review), and result in transforming blue, star-forming galaxies into the ubiquitous red, quiescent galaxies that dominate cluster populations today. These physical processes have been invoked to explain the differences seen in the far-IR–radio relationship as measured between the cluster and field (Murphy et al. 2009a).

However, little work has been done at higher redshifts where we see an increase of star-forming galaxies (Butcher & Oemler 1984), transitional galaxies like E+A (Barger et al. 1996), and AGN (Martini, Sivakoff & Mulchaey 2009) in galaxy clusters. Despite studies looking at the multiwavelength properties of galaxies in distant

*E-mail: solohery@sao.ac.za

clusters (e.g. Best et al. 2002; Saintonge, Tran & Holden 2008), no systematic study has been made of the far-IR–radio relationship in these clusters, and so, the present work is an unique opportunity to explore part of parameter space in *redshift* and *environment* that has not previously been probed.

This work aims to measure the far-IR–radio relation in the massive galaxy cluster MS0451.6-0305 (hereafter MS0451-03) to test how this relationship changes at intermediate redshift between the field and a high-density cluster environment. The properties of the cluster are summarized as follows: MS0451-03 is a massive ($M_{200} \sim 3 \times 10^{15} M_{\odot}$), X-ray luminous ($L_x^{\text{bol}} = 4 \times 10^{45} \text{ erg s}^{-1}$), and large ($R_{200} \sim 2.5 \text{ Mpc}$) cluster at $z = 0.538$ (see Crawford, Bershadsky & Hoessel 2009, table 1).

The paper is organized as follows. Section 2 presents the Very Large Array (VLA) 1.4 GHz radio continuum observations and provides our radio data reduction and analysis. Section 3 presents the *Spitzer* Multiband Imaging Photometer for *Spitzer* (MIPS) observations along with the IR photometry. Sections 4 and 5 describe our sample selection procedure and methodology. Section 6 presents our results. Finally, Sections 7 and 8 discuss and summarize our findings and then suggest some future work. Throughout this paper, we adopt $H_0 = 71 \text{ km s}^{-1} \text{ Mpc}^{-1}$, $\Omega_m = 0.27$, and $\Omega_{\text{DE}} = 0.73$.

2 VLA OBSERVATION AND DATA REDUCTION

2.1 VLA observations

VLA observations at 1.4 GHz were retrieved from the National Radio Astronomy Observatory (NRAO) data archive. The data were all taken in wide field ‘pseudo-continuum mode’ which consists of 25 MHz bandwidth observations acquired at two intermediate frequencies (IFs) centred at 1364.9 and 1435.1 MHz. Each IF consists of seven 3.125 MHz channels and provides both left and right circular polarization. Flux and phase calibration were tracked using flux calibrators (0137+331 or 3C 48) and a phase calibrator (0503+020), respectively. The summary of each archival VLA 1.4 GHz radio continuum observation is provided as follows.

(i) BnA-array¹ data (hereafter B-array) were obtained on 2002 June 9 and 10, that have a sensitivity as reported in the observing log of $\sim 0.052 \text{ mJy beam}^{-1}$ with on-source target durations worth a total observing time of 7.8 h, where data were recorded every 10 s.

(ii) A-array² data were obtained on 2006 February 5–6 and 10–11, that have a sensitivity as reported in the observing log of $\sim 0.04 \text{ mJy beam}^{-1}$ with on-source target durations worth a total observing time of 12.8 h, where data were recorded every 3.3 s.

2.2 VLA data reduction

The radio continuum data reduction and analysis were entirely carried out using the NRAO Astronomical Image Processing System (AIPS) package (Greisen 2003). Our data reduction followed the standard calibration procedures that include data inspection, exploring visibilities, flagging, phase, and flux calibrations. For both B-array and A-array, removal of corrupted data and calibration were performed in a similar manner. The final calibration solutions were applied individually to the different epochs. We combined the two fully calibrated UV data sets and used wide field imaging techniques to image a large field of view beyond the primary beam. We

put facets on all bright sources within one square degrees of the pointing centre to properly account for flux and diminish sidelobe contamination.

Unlike the reduction procedures of Berciano Alba et al. (2010) of this cluster for their studies of sub-mm emissions from galaxies, we treated the B-array observations as a single epoch. No self-calibration was applied. The noise in our combined image was found to be comparable to previously reduced data in the literature. Furthermore, no convolutional artefacts were found around the point sources. The A-array observations were run during the upgrade of the VLA with a mix of Expanded Very Large Array (EVLA) with VLA antennas used during the observing period. As a result, we discarded data from all three EVLA antennas because they could not be calibrated with the VLA antennas.

The A-array data set has higher resolution and is thus quite sensitive to point sources and small structures. Additionally, it dominates the total integrated time on source. As a result, any mapping parameters for the final radio map are dictated by the A-array. Facets for wide field imaging were based on bright sources found by AIPS SETFC routine, resulting in 61 facets that were autogenerated for the targeted field coverage. Each facet was set to the same pixel scaling of 0.3 arcsec and 4096×4096 pixels in size. For all fields, during the cleaning process, cleaned regions were limited to each bright source by putting a clean box around it. The final clean maps have a convolved beam size (HPBW) of $1.99 \text{ arcsec} \times 1.63 \text{ arcsec}$ at a position angle of 0.56. The final flattened radio map was imaged within a field-of-view coverage of 0.75×0.75 with a pixel scaling of 0.3 arcsec and has an rms noise level of $11.98 \mu\text{Jy beam}^{-1}$ as measured using AIPS TVSTAT. We define our detection limit for this image as being $36 \mu\text{Jy}$, which is three times the rms found in a single beam.

2.3 Radio sources extraction and cataloguing

Our radio source catalogue was generated using the AIPS task SAD by running this routine in the signal-to-noise mode ($S/N \geq 3$). The AIPS task RMSD was used to create an rms noise map where calculation of the noise map was performed within a 30 arcsec diameter circular aperture corresponding to 100 neighbour pixels (see e.g. Morrison et al. 2010; Wold et al. 2012). Source classification and flux were assigned based on the method adopted by Owen & Morrison (2008) using the best-fitting major axis value. For the resolved sources (i.e. sources that have a lower-limit best-fitting major axis greater than zero), the total flux densities are directly assigned to the sources while peak flux densities are equal to the total flux densities for the unresolved sources.

We re-measured the 1.4 GHz flux density of fifteen sources published in Wardlow et al. (2010) to verify the quality of our measurements. Within the estimated uncertainty range, we have found a very good consistency between the two measurements with a mean offset of $1.6 \mu\text{Jy}$ and a dispersion of $5.5 \mu\text{Jy}$ (i.e. within the rms noise of our map).

3 SPITZER OBSERVATION AND PHOTOMETRY

3.1 Observations

An MIPS (Rieke et al. 2004) $24 \mu\text{m}$ imaging mosaic for this field was retrieved from the *Spitzer* Enhanced Imaging Products (SEIP³)

¹ Project ID: AN0109, PI: K. Nakanishi.

² Project ID: AB1199, PI: A. Berciano Alba.

³ irsa.ipac.caltech.edu/data/SPITZER/Enhanced/Imaging/

data archive. This high-level product⁴ consists of a combination of multiple programs and has a field of view of $\sim 0.3 \times 0.3$. The mean integration time of the MIPS 24 μm super mosaic imaging is $1637 \text{ s pixel}^{-1}$. The MIPS 24 μm data has a median pixel scaling of 2.45 arcsec and a mean FWHM of 5.9 arcsec. The rms noise of the image was $\sim 26 \mu\text{Jy}$.

Additionally, *Spitzer* super mosaics of the Infrared Array Camera (IRAC; Fazio et al. 2004) at 3.6, 4.5, 5.8, and 8.0 μm were also retrieved. IRAC observations were used for sample selection and matching. The IRAC images have a median pixel scaling of ~ 1.2 arcsec and the image mean FWHM is 1.66, 1.72, 1.88, and 1.98 arcsec, respectively. The rms noise of the images was $\sim 10 \mu\text{Jy}$.

3.2 Far-IR data at longer wavelength

No *Spitzer* MIPS super mosaics imaging at 70 and 160 μm are available in the SEIP data archive for the cluster. However, *Spitzer* MIPS imaging at 24, 70, and 160 μm for the cluster are available in the Spitzer Heritage Archive (SHA⁵) but they have shallower depth and smaller field than the 24 μm images. Due to these limitations, none of the confirmed cluster sources were matched with our 24 μm catalogue. We have examined data from the recently available *Herschel* observations in the field for this cluster which consists of both PACS/PACS Evolutionary Probe (Lutz et al. 2011; Magnelli et al. 2013) and the SPIRE/*Herschel* Multi-tiered Extragalactic Survey (Oliver et al. 2012; Smith et al. 2012). The PACS data do not fully cover our field of view and we were only able to detect two sources in the SPIRE observations. As the *Herschel* data are not expected to significantly modify our results and due to the small number of sources with data, we did not attempt any further analysis using this data. The implications for only including 24 μm observations are further discussed in Section 6.2.

3.3 Photometry

Optical coordinates (see Section 4) were used to perform aperture photometry on the *Spitzer* observations. Aperture photometry was done using APEX (Makovoz & Marleau 2005, *Spitzer* MOPEX). The aperture size was set to a radius of 5.31 arcsec in the MIPS 24 μm imaging, which is the optimal aperture size suggested for point sources based on the pixel sampling of the MIPS 24 μm point spread function.⁶ Clusters sources are expected to be essentially unresolved at this redshift in the MIPS 24 μm data. We re-measured the MIPS 24 μm flux density of the sources published in Wardlow et al. (2010) to verify the quality of our measurements. For 15 sources published in Wardlow et al. (2010), we have found a very good consistency between the two measurements with a mean offset of 16.8 μJy and a dispersion of 46 μJy .

4 SAMPLE SELECTION

Our galaxy sample was drawn based on spectroscopic data of the cluster MS0451-03 (Moran et al. 2007; Crawford et al. 2011) and includes 350 cluster sources. Cluster membership was determined through a ‘shifting-gapper’ analysis (see Crawford, Wirth & Bershadsky 2014) similar to Fadda et al. (1996) which determined membership through analysis of the radius–velocity diagram. Apart from

the confirmed cluster galaxies, our sample also contains 1107 field galaxies that have secure spectroscopic redshift.

Photometry was performed on the MIPS 24 μm image for all spectroscopic sources in our sample appearing in those images. Sources outside of the MIPS 24 μm image were removed from our sample along with sources with flux densities detected at $< 3\sigma$ level. The final catalogue of sources with secure spectroscopic redshifts and IR photometry comprises 155 cluster galaxies and 479 field galaxies.

We matched the radio sources to this catalogue. A matching radius of 2 arcsec was used. Any unambiguous identifications were discarded from the final catalogue. We were able to securely match 12 out of 155 cluster member galaxies and 27 out of 479 field galaxies.

Our full sample of matched sources is presented in Table 1 for cluster galaxies and Table 2 for the field galaxies. The tables include ID, RA, DEC, redshift, radius, 1.4 GHz flux density and its uncertainty, radio luminosity, MIPS 24 μm flux density and its uncertainty, and IR luminosities. As in Yun, Reddy & Condon (2001) and Reddy & Yun (2004), we have not a priori excluded AGN sources so our selection is a heterogeneous sample of star-forming galaxies and AGN. The derivation of the intrinsic properties is presented in Section 5.

5 METHODS

5.1 The radio luminosity

We converted the integrated radio flux densities ($S_{1.4\text{GHz}}$) into rest-frame radio luminosities ($L_{1.4\text{GHz}}$) using

$$L_{1.4\text{GHz}}(\text{W Hz}^{-1}) = \left(\frac{4\pi[D_L(z)]^2}{(1+z)^{1-\alpha}} \right) \times S_{1.4\text{GHz}}, \quad (1)$$

where $S_{1.4\text{GHz}}$ is the flux density at 1.4 GHz in Jy, and $D_L(z)$ is the luminosity distance at the redshift of the sources. The K -correction $1/(1+z)^{(1-\alpha)}$ consists of $1/(1+z)^{-\alpha}$ and $1/(1+z)$ terms that are the ‘colour’ and bandwidth correction, respectively (Morrison et al. 2003). The radio spectral index α is the power-law slope of the synchrotron radiation, and is defined as $S_\nu \sim \nu^{-\alpha}$. We assumed $\alpha \sim 0.8$ for normal star-forming galaxies of Condon (1992).

5.2 The IR luminosities

Since we do not have sufficient information to fit templates to individual galaxies, we used a simple recipe derived from Rieke et al. (2009) for converting between observed 24 μm flux density and $L_{24\mu\text{m}}$ based on the best-fitting SFR calibration. This is based on equations 10–14 and table 1 from Rieke et al. (2009). The conversion is as follows:

$$L(24\mu\text{m}, L_\odot) = \frac{10^{A(z)+B(z) \times (\log(4\pi D_L^2 f_{24,\text{obs}}) - 53)}}{7.8 \times 10^{-10}}; \quad (2)$$

for, $6 \times 10^8 L_\odot \leq L_{24\mu\text{m}} \leq 1.3 \times 10^{10} L_\odot$

$$L(24\mu\text{m}, L_\odot) = \left(\frac{10^{A(z)+B(z) \times (\log(4\pi D_L^2 f_{24,\text{obs}}) - 53)}}{7.8 \times 10^{-10} \times (7.76 \times 10^{-11})^{0.048}} \right)^{0.954}; \quad (3)$$

if, $L_{24\mu\text{m}} > 1.3 \times 10^{10} L_\odot$,

where D_L is the luminosity distance in cm and $f_{24,\text{obs}}$ is the flux density at 24 μm in Jy. The coefficients $A(z)$ and $B(z)$ are redshift

⁴ ADS/IRSA.Atlas#2013/0325/072424_12320

⁵ sha.ipac.caltech.edu/applications/Spitzer/SHA/

⁶ irsa.ipac.caltech.edu/data/SPITZER/docs/

Table 1. Properties of cluster galaxies that include the total IR luminosity (L_{TIR}) and rest-frame radio luminosity ($L_{1.4\text{GHz}}$).

ID	RA (Degree)	DEC (Degree)	Redshift	R (Mpc)	$S_{1.4}$ (μJy)	$S_{1.4\text{-err}}$ (μJy)	$\log L_{1.4}$ (W Hz^{-1})	S_{24} (mJy)	$S_{24\text{-err}}$ (mJy)	$\log(L_{24\mu\text{m}})$ (L_{\odot})	$\log(L_{60\mu\text{m}})$ (L_{\odot})	$\log(L_{\text{FIR}})$ (L_{\odot})	$\log(L_{\text{TIR}})$ (L_{\odot})		
1081	73.514	153	−2.988	997	0.531	0.927	75.906	24.331	22.893	0.323	0.027	10.364	10.931	10.938	11.239
1093	73.521	263	−2.994	204	0.527	0.728	144.311	21.045	23.164	0.357	0.027	10.405	10.973	10.977	11.278
1118	73.518	738	−3.003	781	0.532	0.656	134.7	25.47	23.144	0.363	0.027	10.427	10.995	10.998	11.299
1143	73.516	792	−2.990	292	0.532	0.863	116.476	24.413	23.080	0.307	0.027	10.339	10.904	10.914	11.215
1158	73.520	401	−3.000	317	0.542	0.660	156.083	24.667	23.226	0.156	0.027	10.002	10.559	10.596	10.897
1178	73.523	178	−2.988	423	0.530	0.794	183.027	54.111	23.273	0.286	0.027	10.295	10.860	10.873	11.174
1489	73.534	897	−3.054	384	0.548	0.905	60.155	20.114	22.824	0.846	0.027	10.914	11.495	11.457	11.758
1726	73.549	652	−3.044	432	0.541	0.658	862.685	98.963	23.966	0.084	0.027	9.661	10.208	10.274	10.575
1811	73.550	758	−3.016	844	0.539	0.132	36.000	12.000	22.585	0.170	0.023	10.045	10.602	10.636	10.937
2143	73.558	327	−3.033	125	0.544	0.495	40.246	14.39	22.643	0.121	0.026	9.871	10.424	10.472	10.774
7240	73.551	170	−3.016	482	0.539	0.140	46.558	13.505	22.696	0.216	0.023	10.172	10.734	10.757	11.058
8110	73.396	484	−3.020	605	0.536	3.370	255.464	73.437	23.429	0.897	0.021	10.914	11.495	11.457	11.758

Table 2. Properties of field galaxies that include the total IR luminosity (L_{TIR}) and rest-frame radio luminosity ($L_{1.4\text{GHz}}$).

ID	RA (Degree)	DEC (Degree)	Redshift	R (Mpc)	$S_{1.4}$ (μJy)	$S_{1.4\text{-err}}$ (μJy)	$\log L_{1.4}$ (W Hz^{-1})	S_{24} (mJy)	$S_{24\text{-err}}$ (mJy)	$\log(L_{24\mu\text{m}})$ (L_{\odot})	$\log(L_{60\mu\text{m}})$ (L_{\odot})	$\log(L_{\text{FIR}})$ (L_{\odot})	$\log(L_{\text{TIR}})$ (L_{\odot})		
1046	73.513	374	−2.989	720	0.578	0.930	1099.165	125.937	24.141	0.260	0.027	10.368	10.935	10.942	11.243
1743	73.547	653	−3.042	384	0.586	0.606	64.228	16.439	22.922	0.091	0.027	9.824	10.375	10.427	10.728
1937	73.550	400	−3.057	221	0.655	0.947	1530.335	260.189	24.414	0.314	0.027	10.621	11.195	11.181	11.482
2472	73.570	877	−3.027	037	0.617	0.639	307.426	28.24	23.654	0.359	0.026	10.622	11.196	11.182	11.483
2818	73.587	166	−2.987	284	0.239	1.153	114.59	31.547	22.273	0.317	0.029	9.299	9.836	9.931	10.232
2912	73.586	548	−2.998	683	0.725	1.018	79.373	25.822	23.233	0.193	0.030	10.475	11.044	11.043	11.344
3017	73.591	164	−2.990	986	0.489	1.187	109.072	34.843	22.967	0.110	0.036	9.664	10.211	10.276	10.577
3226	73.603	012	−2.980	324	0.725	1.541	656.767	39.495	24.150	0.198	0.040	10.491	11.060	11.058	11.359
3462	73.610	458	−2.947	674	0.728	2.141	220.184	38.439	23.680	0.172	0.039	10.418	10.986	10.989	11.290
3806	73.626	404	−2.999	176	0.332	1.883	210.369	38.786	22.860	1.336	0.034	10.461	11.030	11.030	11.331
3957	73.619	141	−2.937	129	0.323	2.450	192.012	58.31	22.795	1.741	0.032	10.562	11.134	11.125	11.426
5823	73.624	580	−2.969	661	0.447	2.084	153.757	41.791	23.023	0.472	0.033	10.326	10.891	10.902	11.203
6380	73.580	307	−2.921	304	0.619	2.286	245.952	45.472	23.561	0.453	0.013	10.750	11.327	11.302	11.603
6638	73.648	750	−2.975	052	0.447	2.526	390.0	50.734	23.427	0.834	0.021	10.625	11.199	11.185	11.486
7372	73.573	524	−2.971	213	0.777	1.199	113.395	31.084	23.460	0.149	0.027	10.415	10.982	10.986	11.287
8060	73.394	081	−3.050	711	0.491	3.513	213.045	73.092	23.261	0.074	0.022	9.450	9.992	10.074	10.375
8134	73.402	657	−3.035	359	0.715	3.258	312.974	74.698	23.814	0.329	0.023	10.753	11.330	11.306	11.607
8415	73.586	739	−3.150	578	0.505	3.199	224.847	63.553	23.313	0.240	0.013	10.138	10.699	10.725	11.026
8575	73.623	688	−2.891	933	0.900	3.326	2337.128	397.688	24.927	0.454	0.022	11.324	11.916	11.845	12.146
8578	73.655	594	−2.971	230	0.802	2.702	247.537	53.255	23.832	0.864	0.021	11.459	12.056	11.973	12.274
8581	73.659	332	−2.969	704	0.219	2.794	115.513	41.055	22.191	1.068	0.022	9.818	10.370	10.422	10.723
8583	73.648	529	−2.962	799	0.590	2.636	156.628	50.165	23.315	0.788	0.025	10.979	11.562	11.519	11.820
8608	73.670	662	−2.991	703	0.447	2.900	183.367	62.913	23.099	0.474	0.022	10.327	10.893	10.903	11.204
8631	73.664	940	−3.052	018	0.794	2.840	205.325	56.57	23.741	0.477	0.021	11.104	11.691	11.637	11.938
8642	73.693	115	−3.053	544	0.280	3.464	188.581	69.843	22.646	0.749	0.025	9.942	10.497	10.539	10.840
8773	73.578	003	−2.830	110	0.491	4.275	239.729	85.027	23.312	0.789	0.026	10.725	11.301	11.279	11.580
8813	73.656	097	−2.904	510	0.756	3.564	229.033	67.389	23.736	0.312	0.023	10.796	11.374	11.346	11.647

dependent and can be obtained by interpolating the values in table 1 of Rieke et al. (2009); or see values are provided in our Table A1 in Appendix A.

In addition to $L_{24\mu\text{m}}$, we also calculate the IR luminosities L_{TIR} , $L_{60\mu\text{m}}$, and L_{FIR} to allow a comparison of our measurements to other works. We adopt the definition from Rieke et al. (2009) that L_{TIR} is the luminosity between $L(\text{TIR}; 8\text{--}1000\mu\text{m})$, and we adopt the definition of L_{FIR} from Helou et al. (1985) as $L(\text{FIR}; 42\text{--}122\mu\text{m})$. We provide the details of these transformations in Appendix A.

We also attempted to determine L_{TIR} based on fitting the spectral energy distribution (SED) using CIGALE⁷ (Noll et al. 2009). The photometric catalogues were fitted to synthetic template spectra

compiled from Maraston (2005) that incorporate the dust-emission model of Dale & Helou (2002). The total IR luminosities were then derived from the parameters of the best-fitting model. Due to lacking suitable measurements in bandpasses that are redwards of $24\mu\text{m}$, the scarcity of data points, and the large parameter space of models, our measurements of the total IR luminosity L_{TIR} were poorly constrained. We thus limited any further analysis to the empirically determined L_{TIR} .

5.3 The IR to radio luminosity ratio

We characterized the quantitative measure of the far-IR–radio relation by calculating the median logarithmic ratio of IR and radio

⁷ <http://cigale.oamp.fr/>

luminosity (q). The luminosity ratio was estimated using the commonly used equation of Helou et al. (1985) as follows:

$$q = \log\left(\frac{L}{3.75 \times 10^{12} \text{ W}}\right) - \log\left(\frac{L_{1.4\text{GHz}}}{\text{W Hz}^{-1}}\right), \quad (4)$$

where $L_{1.4\text{GHz}}$ is the rest-frame radio luminosity calculated from equation (1) in W Hz^{-1} . L is our IR luminosity in W . The subscript of q indicates which IR luminosity is being used (i.e. q_{TIR} is for L_{TIR}). For calculating q_{24} , the constant used to normalize the IR luminosity was 1.25×10^{13} .

6 RESULTS

Our primary aim is to compare the IR–radio relationship in an intermediate-redshift cluster to nearby clusters, and to do so, we will be comparing our results to the lower redshift measurements of Reddy & Yun (2004). As their results are reported in $L_{60\mu\text{m}}$ and q_{FIR} within L_{FIR} (42–122 μm), we transform our $L_{24\mu\text{m}}$ results into comparable bands. We report the luminosities for all the cluster sources in Table 1 and field sources in Table 2.

6.1 Far-IR–radio relation

The relationship between the rest-frame radio luminosity at 1.4 GHz ($L_{1.4\text{GHz}}$) against the IR luminosity ($L_{60\mu\text{m}}$) is shown in Fig. 1. The solid line indicates the formal linear least-squares fit of the cluster galaxies of Reddy & Yun (2004) while the field relation from Yun et al. (2001) is drawn using the dashed line. Most of our cluster sources are consistent with these relationships. As indicated in the dash-dotted lines in Fig. 1, our cluster galaxies IR luminosity and radio luminosity lower limits are $\log L_{60\mu\text{m}} = 10.21$ and $\log L_{1.4\text{GHz}} = 22.6$, respectively. For comparison, our lower limits

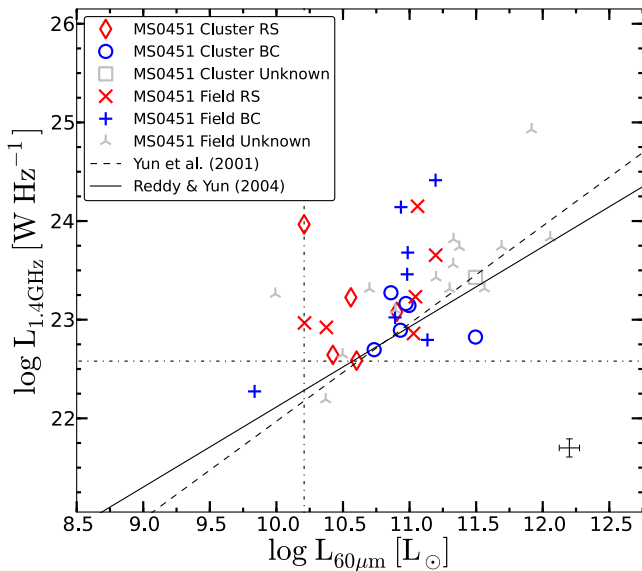


Figure 1. The 20 cm radio continuum luminosity ($L_{1.4\text{GHz}}$) against the IR luminosity ($L_{60\mu\text{m}}$). Red colour indicates RS galaxies while blue colour represents BC galaxies. RS field galaxies are plotted in cross symbols, while BC field galaxies are drawn in plus symbols. Grey colour represents sources with unknown photometric classification. The solid and dashed lines indicate the formal linear least-squares fit ($\log L_{60\mu\text{m}} = 8.92$ luminosity cutoff) of the low-redshift cluster galaxies from Reddy & Yun (2004) and field galaxies relation in equation 4 of Yun et al. (2001). The error bars correspond to average 1σ errors.

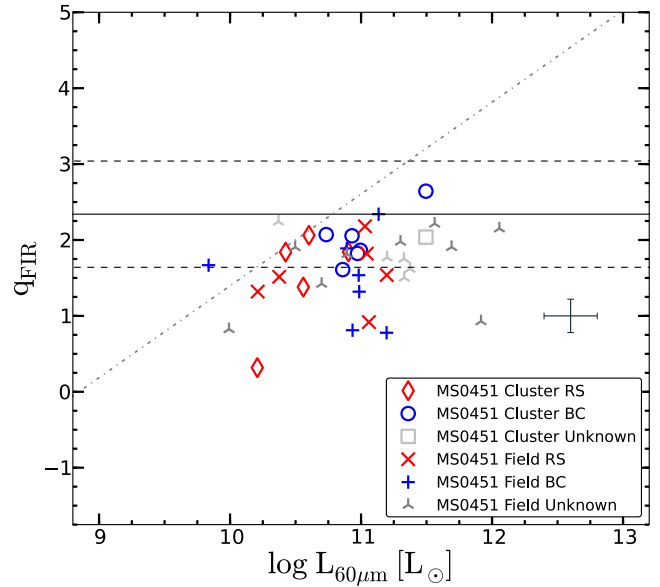


Figure 2. The logarithm of the far-IR luminosity to 1.4 GHz radio continuum luminosity ratio (q_{FIR}) versus the IR luminosity ($L_{60\mu\text{m}}$). The nominal value of q_{FIR} for field galaxies ($q_{\text{FIR}} = 2.34$) is plotted in the solid black horizontal line. The criteria for both delineating the radio-excess ($q_{\text{FIR}} \leq 1.64$) and IR-excess ($q_{\text{FIR}} \geq 3.04$) are shown in the dashed lines. The error bars correspond to average 1σ errors. The solid grey line represents our sample-limiting flux.

are higher than the low-redshift cluster galaxies ($\log L_{60\mu\text{m}} = 8.92$, $\log L_{1.4\text{GHz}} = 20.47$) of Reddy & Yun (2004).

We split our sample into blue cloud (BC) and red sequence (RS) galaxies following the definition in Crawford et al. (2011) for both cluster and field samples. In all the figures, red and blue colours indicate sources that have secure photometric measurements from our imaging data, while grey colour represents sources with unknown photometric classification. The number of sources that have secure photometric classification is 11 of 12 cluster sources and 13 of 27 field sources. For any values given for these populations, we only use sources with secure photometric measurements. For all other values reported in this paper, we calculate them based on the full cluster or field sample.

In Fig. 2, we present the far-IR luminosity (L_{FIR}) to radio luminosity ($L_{1.4\text{GHz}}$) ratio (q_{FIR}) versus $L_{60\mu\text{m}}$. The solid grey line delineates our sample-limiting magnitude. The mean q_{FIR} for the cluster population is $q_{\text{FIR}} = 1.80 \pm 0.15$ with a dispersion of 0.53, while field galaxies have $q_{\text{FIR}} = 1.62 \pm 0.09$ with a dispersion of 0.45. Our cluster value is consistent with Reddy & Yun (2004) value of $q_{\text{FIR}} = 2.07 \pm 0.07$ with a dispersion of 0.74. Our field value is lower, but due to the large intrinsic dispersion, we cannot firmly comment on its inconsistency with values found in similar works such as Yun et al. (2001) of $q_{\text{FIR}} = 2.34 \pm 0.01$ with a dispersion of 0.26. In addition to Reddy & Yun (2004) and Yun et al. (2001), our mean q_{FIR} values are comparable with other works (Andersen & Owen 1995; Miller & Owen 2001; Garrett 2002; Kovács et al. 2006; Sajina et al. 2008; Murphy et al. 2009a); see Table A2 for values from each of the surveys.

We also compare our other measurements to other works as well. For comparison, we found mean values of $q_{24} = 0.69 \pm 0.16$ with a dispersion of 0.55 and $q_{\text{TIR}} = 2.10 \pm 0.15$ with a dispersion of 0.53 for cluster sources while $q_{24} = 0.52 \pm 0.09$ with a dispersion of 0.46 and $q_{\text{TIR}} = 1.92 \pm 0.09$ with a dispersion of 0.45 for our field

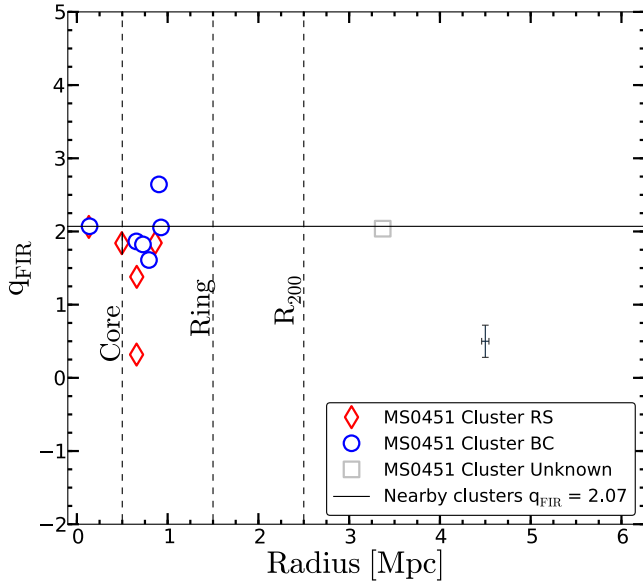


Figure 3. Plot of the galaxy-projected radius against the far-IR to radio luminosity ratio q_{FIR} . The mean value of q_{FIR} for low-redshift cluster galaxies of Reddy & Yun (2004) is shown in the solid horizontal line ($q_{\text{FIR}} = 2.07$). Similar to Reddy & Yun (2004), the vertical dashed lines define the R_{Core} , R_{Ring} as the projected cluster-centric distance at $R \leq 0.5$ and between $[0.5, 1.5]$ Mpc, respectively. The error bars correspond to average 1σ errors.

sources. A comparison of q_{24} and q_{TIR} values in the field indicates that our values are consistent with previously published values of q_{24} (Appleton et al. 2004; Murphy et al. 2006; Beswick et al. 2008; Ibar et al. 2008; Garn et al. 2009) and q_{TIR} (Murphy et al. 2009b; Ivison et al. 2010a,b; Jarvis et al. 2010).

As for the low-redshift environment, the field and cluster q_{FIR} are consistent, although with the large dispersions measured for our small sample, it is difficult to notice any significant differences. The field sample shows a strong bias with redshift (with more excess objects at higher redshift) and as such, we exclude it from further analysis. The q -value will be further discussed in Section 7.

In addition, Fig. 2 shows that most sources lie within the adopted range defined as radio-excess ($q_{\text{FIR}} \leq 1.64$) and IR-excess ($q_{\text{FIR}} \geq 3.04$) by Yun et al. (2001) as shown by the dashed lines. A radio (IR) excess galaxy is defined to have at least five times greater radio (IR) flux than what is expected from the field galaxy at that redshift for a given far-IR luminosity. We find that the percentage⁸ of cluster galaxies that have radio-excess are 27^{+23}_{-13} per cent. The number of radio-excess cluster members is higher than the percentage found by Reddy & Yun (2004, $11^{+1.7}_{-4.7}$ per cent) for low-redshift clusters.

Out of the cluster population, two of five (40 per cent) RS galaxies are radio-excess sources. In their sample, Reddy & Yun (2004) find 28 per cent of cluster early-type galaxies show a radio-excess and that all also display evidence of AGN activity. For the BC cluster galaxies, we find one of six (16 per cent) radio-excess sources, which is consistent with the results of Miller & Owen (2001) and Reddy & Yun (2004). For these blue population, where $q_{\text{FIR}} = 2.01 \pm 0.14$ with a dispersion of 0.35, which is consistent with the field at low redshift and intermediate redshift.

In Fig. 3, we plotted the far-IR and radio luminosity ratio (q_{FIR}) as a function of the galaxy-projected radius R in Mpc. In aiming to use radius as a proxy for local density, similar to Reddy & Yun (2004),

⁸ Errors for percentages were calculated following Gehrels (1986).

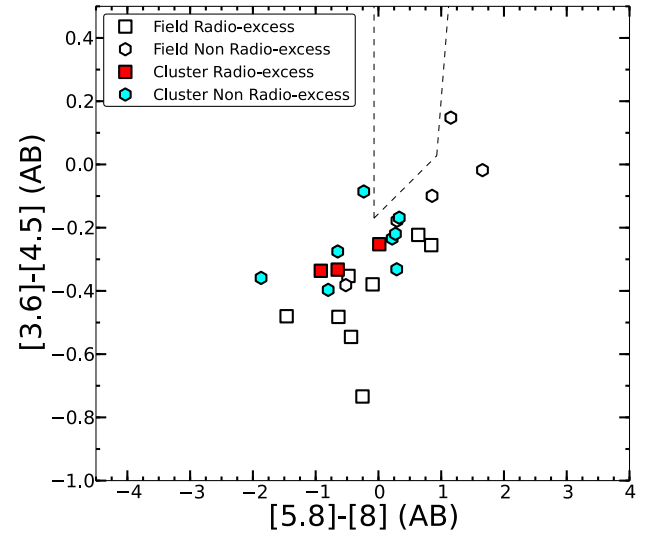


Figure 4. Plot of AGN indices. IRAC colour-colour diagnostic for AGN.

we defined R_{Core} , R_{Ring} as the projected cluster-centric distance at $R \leq 0.5$ Mpc and between $[0.5, 1.5]$ Mpc, respectively. Miller & Owen (2001) and Reddy & Yun (2004) find a higher fraction of core galaxies that have a radio-excess, but we see no evidence of this in our sample drawn from one cluster.

6.2 Potential caveats

Before interpreting our findings, there are some caveats related to the derived luminosities which need to be considered.

6.2.1 Far-IR–radio relation: presence of AGN

For comparison purposes and conformity to the previous work in the literature (Reddy & Yun 2004), we do not a priori exclude AGN, but analyse both star-forming galaxies and AGN together. It has been established that faint radio populations are mostly found to be composed of star-forming galaxies and radio-quiet AGN (e.g. Jarvis & Rawlings 2004). It is also acknowledged that there is generally a contribution to the net radio flux from an AGN which can affect the observed relationship. However, we do note that the optical spectra for our sources do not show evidence of AGN activity based on the lack of broad-line sources. We then followed the method of Stern et al. (2005) to check for AGN contamination using IRAC colour-colour plots which is shown in Fig. 4. We particularly adopted the formulation in AB mag system by Messias et al. (2010) as shown in their fig. 4. We find no clusters sources that show any indication of being an AGN according to the classification as defined by Stern et al. (2005) and Messias et al. (2010). The implications of AGN in our sample are further discussed in Section 7.

6.2.2 IR luminosity derived from 24 μm

Observations at 24 μm may not be providing an unbiased estimator of the star formation since the peak of the IR SED tracing the cold dust component peaks between 60 and 170 μm (Pierini et al. 2003). Furthermore, 24 μm data may be affected by dust heating from older stellar populations (Calzetti et al. 2010), although the 24 μm flux is going to be dominated by the warm dust component.

In addition, there is an order of a magnitude correction required to convert 24 μm flux to total IR flux, which small scatter in the relationship can contribute large uncertainties. However, Dale et al.

(2001) argued that 20–42 μm is essentially a good tracer of the bulk of dust emission and hence can be a robust recent star formation indicator. Recent studies of the relationship in the field have also found consistent results between mid-IR MIPS 24 μm and MIPS 70 μm results (e.g. Appleton et al. 2004; Beswick et al. 2008). In addition, Murphy et al. (2011) find that 24 μm observations are a sufficient tracer of the total IR luminosity of galaxies for galaxies with $L_{24\mu\text{m}} < 10^{12} L_{\odot}$, which includes all of our cluster sample.

Galamez et al. (2013) combined *Spitzer* and *Herschel* data and noted that an inclusion of 24 μm wavelength is essential in order to robustly derive the total IR luminosity for nearby star-forming galaxies. In addition, for luminous galaxies at $z < 1.3$, measurement based on mid-IR is in agreement with those measured directly with *Herschel*, as already shown by Elbaz et al. (2011).

6.2.3 Small sample size

Given the fact that we have studied only one cluster containing a relatively small number of members, it is important to note that the current results may suffer from small sample size. In our sample, we did not detect the brightest cluster galaxy (which is obscured by a foreground galaxy) while Reddy & Yun (2004) have four cDs in their sample.

7 DISCUSSIONS

Among the low-redshift cluster studies, the far-IR–radio relationship in rich cluster galaxies is characterized by a lower value of q_{FIR} as compared to the field that is indicative of an excess of radio emission. Cluster environmental effects are believed to drive these observations (Andersen & Owen 1995; Rengarajan, Karnik & Iyengar 1997). Andersen & Owen (1995) postulated that the interstellar medium (ISM) of galaxies in rich clusters is being compressed via ram pressure as the galaxies move through the intracluster medium (ICM) resulting in greater radio emission. More recent work has further examined various models to shed some light on the causes of enhanced radio emission that seems globally present in cluster galaxies (Miller & Owen 2001; Reddy & Yun 2004; Murphy et al. 2009a). The most common scenarios include thermal pressure compression by the ICM and the ram pressure stripping of ISM, which are both likely to augment the galactic magnetic field.

If we compare our results with the study of low-redshift clusters by Reddy & Yun 2004, we find the following: (1) the intermediate-redshift cluster sample has a lower value of $q_{\text{FIR}} = 1.80 \pm 0.15$ with a dispersion of 0.53, but one that is consistent within the dispersion with the low-redshift clusters where $q_{\text{FIR}} = 2.07 \pm 0.07$ with a dispersion of 0.74; (2) the fraction of radio-excess objects in clusters at intermediate redshifts is greater than in the low redshift (27^{+23}_{-13} per cent to 11 per cent); (3) we find no preference for radio-excess objects in the cluster core. However, we caution that any results from this work may suffer from the small sample size studied here.

Our measurement of q_{TIR} in the field at intermediate redshift is consistent with previous work (Murphy et al. 2009b; Ivison et al. 2010a,b; Jarvis et al. 2010), and little or no evolution has been reported in the evolution of the q_{TIR} value in the field at these redshifts (e.g. Ivison et al. 2010b; Sargent et al. 2010a,b; Bourne et al. 2011). However, the significant increase in the scatter in the q_{FIR} value is inconsistent with these works as well as the scattered measured by Yun et al. (2001) at low redshift. The high scatter that we are measuring may be due to preferentially selecting radio-bright objects especially at higher redshift. For this

reason, we will focus on the observed fraction of radio-excess objects seen in the cluster and the behaviour of blue galaxies in the cluster.

In the intermediate-redshift cluster, we observe a higher fraction of radio-excess galaxies as compared to lower redshift. Two thirds of the sources classified as radio-excess sources are RS galaxies. Reddy & Yun (2004) found that 9 of 13 excess sources at low redshift had AGN signatures and were early-type galaxies. From visual inspection of their spectra and analysis of their mid-IR colours, our two red galaxies do not show broad emission lines or other telltale AGN signatures, but their large offset from the relationship may be indicative of nuclear activity. As can be seen in Fig. 2, most of the blue galaxies appear normal and have a very small scatter in their q_{FIR} values. We find one blue galaxy showing a radio-excess.

In Fig. 3, we do not see any strong radial trends against the q_{FIR} values. However, we notice that there is a significant scatter within the ring galaxies. Overall, inspection of the median q_{FIR} value indicates that the far-IR–radio relation for cluster blue galaxies at $z \sim 0.5$ is similar to the cluster sample at low redshift.

At low-redshift clusters, one interpretation of the presence of radio-excess within the virial radius can be the results of ISM stripped off via ram pressure exerted by infalling galaxies. We do not see any strong environmental effects in the value of q_{FIR} at these redshifts, although we do see a greater percentage of excess objects. It is possible that the quenching mechanism is different than it is at low redshift although a larger sample would be required to verify this. Follow-up observations of these excess objects found at intermediate redshift clusters would also help in exploring their properties.

However, we note that the radio spectral index α depends on frequency and galaxy properties and thus using a single spectral index may also alter the value of q (e.g. Bourne et al. 2011). However, the majority of work of this kind has been using the standard spectral index for normal star-forming galaxies; $\alpha \sim 0.8$ of Condon (1992). Recent results from the local IR luminous galaxies of Murphy et al. (2013) found that the mid-IR and radio properties of star-forming galaxies, particularly for those compact starburst galaxies, tend to have a flatter ($\alpha \sim 0.5$) spectral index. This may be a concern for galaxies in clusters as Crawford et al. (2006, 2011) find an increase in compact galaxies in clusters at these redshifts. The recently upgraded VLA correlator now makes it possible to measure the spectral index over a wide bandwidth within a single observation, so it will be a powerful tool for determining the IR–radio relation for large field and cluster samples in the future.

8 CONCLUSION

We have studied the far-IR–radio relation in the massive galaxy cluster MS0451-03 and investigated, for the first time, how this relationship behaves at intermediate redshift between the field and a high-density cluster environment. We have constructed the far-IR–radio relationship of star-forming galaxies using deep VLA and *Spitzer* archival data. We have measured the rest-frame radio luminosity at 1.4 GHz and the total IR luminosity ratios for both sample of confirmed MS0451-03 cluster and field galaxies.

We find that the far-IR–radio relationship for distant cluster populations ($q_{\text{FIR}} = 1.80 \pm 0.15$ with a dispersion of 0.53) is in agreement with those measured in low-redshift clusters ($q_{\text{FIR}} = 2.07 \pm 0.07$ with a dispersion of 0.74). We do find an evidence for a cluster enhancement of the radio-excess sources with the value in MS0451-03 (27^{+23}_{-13} per cent) being significantly higher than that in low-redshift

clusters ($11^{+1.7}_{-4.7}$ per cent). In addition, the far-IR–radio relationship for blue galaxies, where $q_{\text{FIR}} = 2.01 \pm 0.14$ with a dispersion of 0.35, is consistent with the predicted value from the field relationship, although these results are based on a sample from a single cluster. We find one radio-excess galaxy among the blue star-forming galaxies and two RS galaxies with radio-excess. Unlike low-redshift galaxies, our galaxies do not show any evidence of AGN activity, but further observations will be needed to confirm the nature of these objects. We do not find any trends with radius for radio-excess populations within this one cluster.

In future work, we will expand our sample of distant and rich clusters to further explore the relationship at intermediate redshift. The subsequent analysis of the extended sample shall provide higher statistics and will allow further confirmation of differences seen between low and intermediate redshift.

ACKNOWLEDGEMENTS

We would like to thank the anonymous referee for his/her thorough review of our manuscript and the valuable comments. We thank Dr Elodie Giovannoli for her helpful discussions and suggestions. SMR and MV were supported by the South African Square Kilometre Array Project (SKA SA) and the National Research Foundation (NRF). SMR wishes to thank the South African Astronomical Observatory NRF/SAAO for their support. KMH's research has been supported by the South African Research Chairs Initiative (SARChI) of the Department of Science and Technology (DST), the SKA SA and the NRF.

We are grateful to the W. M. Keck Observatory for the observations. The NRAO is a facility of the National Science Foundation operated under cooperative agreement by Associated Universities, Inc. This research has made use of the NASA/IPAC Infrared Science Archive, which is operated by the Jet Propulsion Laboratory, California Institute of Technology, under contract with the National Aeronautics and Space Administration: ADS/IRSA.Atlas#2013/0325/072424_12320.

REFERENCES

- Andersen V., Owen F. N., 1995, *AJ*, 109, 1582
 Appleton P. N. et al., 2004, *ApJS*, 154, 147
 Barger A. J., Aragon-Salamanca A., Ellis R. S., Couch W. J., Smail I., Sharples R. M., 1996, *MNRAS*, 279, 1
 Bell E. F., 2003, *ApJ*, 586, 794
 Berciano Alba A., Koopmans L. V. E., Garrett M. A., Wucknitz O., Limousin M., 2010, *A&A*, 509, A54
 Best P. N., van Dokkum P. G., Franx M., Röttgering H. J. A., 2002, *MNRAS*, 330, 17
 Beswick R. J., Muxlow T. W. B., Thrall H., Richards A. M. S., Garrington S. T., 2008, *MNRAS*, 385, 1143
 Boselli A., Gavazzi G., 2006, *PASP*, 118, 517
 Bourne N., Dunne L., Ivison R. J., Maddox S. J., Dickinson M., Frayer D. T., 2011, *MNRAS*, 410, 1155
 Boyle B. J., Cornwell T. J., Middelberg E., Norris R. P., Appleton P. N., Smail I., 2007, *MNRAS*, 376, 1182
 Butcher H., Oemler A., Jr, 1984, *ApJ*, 285, 426
 Calzetti D. et al., 2010, *ApJ*, 714, 1256
 Condon J. J., 1992, *ARA&A*, 30, 575
 Condon J. J., Anderson M. L., Helou G., 1991, *ApJ*, 376, 95
 Crawford S. M., Bershady M. A., Glenn A. D., Hoessel J. G., 2006, *ApJ*, 636, L13
 Crawford S. M., Bershady M. A., Hoessel J. G., 2009, *ApJ*, 690, 1158
 Crawford S. M., Wirth G. D., Bershady M. A., Hon K., 2011, *ApJ*, 741, 98
 Crawford S. M., Wirth G. D., Bershady M. A., 2014, *ApJ*, 786, 30
 Dale D. A., Helou G., 2002, *ApJ*, 576, 159
 Dale D. A., Helou G., Contursi A., Silbermann N. A., Kolhatkar S., 2001, *ApJ*, 549, 215
 Elbaz D. et al., 2011, *A&A*, 533, A119
 Fadda D., Girardi M., Giuricin G., Mardirossian F., Mezzetti M., 1996, *ApJ*, 473, 670
 Fazio G. G. et al., 2004, *ApJS*, 154, 10
 Galametz M. et al., 2013, *MNRAS*, 431, 1956
 Garn T., Green D. A., Riley J. M., Alexander P., 2009, *MNRAS*, 397, 1101
 Garrett M. A., 2002, *A&A*, 384, L19
 Gehrels N., 1986, *ApJ*, 303, 336
 Greisen E. W., 2003, *Astrophys. Space Sci. Libr.*, 285, 109
 Helou G., Soifer B. T., Rowan-Robinson M., 1985, *ApJ*, 298, L7
 Helou G., Khan I. R., Malek L., Boehmer L., 1988, *ApJS*, 68, 151
 Ibar E. et al., 2008, *MNRAS*, 386, 953
 Ivison R. J. et al., 2010a, *MNRAS*, 402, 245
 Ivison R. J. et al., 2010b, *A&A*, 518, L31
 Jarvis M. J., Rawlings S., 2004, *New Astron. Rev.*, 48, 1173
 Jarvis M. J. et al., 2010, *MNRAS*, 409, 92
 Kovács A., Chapman S. C., Dowell C. D., Blain A. W., Ivison R. J., Smail I., Phillips T. G., 2006, *ApJ*, 650, 592
 Lutz D. et al., 2011, *A&A*, 532, A90
 Magnelli B. et al., 2013, *A&A*, 553, A132
 Makovoz D., Marleau F. R., 2005, *PASP*, 117, 1113
 Maraston C., 2005, *MNRAS*, 362, 799
 Martini P., Sivakoff G. R., Mulchaey J. S., 2009, *ApJ*, 701, 66
 Messias H., Afonso J., Hopkins A., Mobasher B., Dominici T., Alexander D. M., 2010, *ApJ*, 719, 790
 Miller N. A., Owen F. N., 2001, *AJ*, 121, 1903
 Moran S. M., Ellis R. S., Treu T., Smith G. P., Rich R. M., Smail I., 2007, *ApJ*, 671, 1503
 Morrison G. E., Owen F. N., Ledlow M. J., Keel W. C., Hill J. M., Voges W., Herter T., 2003, *ApJS*, 146, 267
 Morrison G. E., Owen F. N., Dickinson M., Ivison R. J., Ibar E., 2010, *ApJS*, 188, 178
 Murphy E. J., 2009, *ApJ*, 706, 482
 Murphy E. J. et al., 2006, *ApJ*, 638, 157
 Murphy E. J., Kenney J. D. P., Helou G., Chung A., Howell J. H., 2009a, *ApJ*, 694, 1435
 Murphy E. J., Chary R.-R., Alexander D. M., Dickinson M., Magnelli B., Morrison G., Pope A., Teplitz H. I., 2009b, *ApJ*, 698, 1380
 Murphy E. J., Chary R.-R., Dickinson M., Pope A., Frayer D. T., Lin L., 2011, *ApJ*, 732, 126
 Murphy E. J., Stierwalt S., Armus L., Condon J. J., Evans A. S., 2013, *ApJ*, 768, 2
 Noll S., Burgarella D., Giovannoli E., Buat V., Marcellac D., Muñoz-Mateos J. C., 2009, *A&A*, 507, 1793
 Oliver S. J. et al., 2012, *MNRAS*, 424, 1614
 Owen F. N., Morrison G. E., 2008, *AJ*, 136, 1889
 Pierini D., Popescu C. C., Tuffs R. J., Völk H. J., 2003, *A&A*, 409, 907
 Reddy N. A., Yun M. S., 2004, *ApJ*, 600, 695
 Rengarajan T. N., Karnik A. D., Iyengar K. V. K., 1997, *MNRAS*, 290, 1
 Rieke G. H. et al., 2004, *ApJS*, 154, 25
 Rieke G. H., Alonso-Herrero A., Weiner B. J., Pérez-González P. G., Blaylock M., Donley J. L., Marcellac D., 2009, *ApJ*, 692, 556
 Saintonge A., Tran K.-V. H., Holden B. P., 2008, *ApJ*, 685, L113
 Sajina A. et al., 2008, *ApJ*, 683, 659
 Sanders D. B., Mirabel I. F., 1996, *ARA&A*, 34, 749
 Sanders D. B., Mazzarella J. M., Kim D.-C., Surace J. A., Soifer B. T., 2003, *AJ*, 126, 1607
 Sargent M. T. et al., 2010a, *ApJS*, 186, 341
 Sargent M. T. et al., 2010b, *ApJ*, 714, L190
 Smith A. J. et al., 2012, *MNRAS*, 419, 377
 Stern D. et al., 2005, *ApJ*, 631, 163
 van der Kruit P. C., 1971, *A&A*, 15, 110
 Wardlow J. L. et al., 2010, *MNRAS*, 401, 2299
 Wold I. G. B., Owen F. N., Wang W.-H., Barger A. J., Keenan R. C., 2012, *ApJS*, 202, 2

Younger J. D. et al., 2009, MNRAS, 394, 1685
 Yun M. S., Reddy N. A., Condon J. J., 2001, ApJ, 554, 803

APPENDIX A: EQUATIONS USED TO ESTIMATE IR LUMINOSITIES

Additional materials are provided in this Appendix which consists of empirical relations used to estimate IR luminosities and a table that contains various q -values in the literature (See Table A2).

Table A1. SFR(flux) fit coefficients A and B as a function of redshift for MIPS. $A(z)$ and $B(z)$ are to be used in equations (2) and (3) as the intercept and slope of the relation of SFR on observed IR flux (see Rieke et al. 2009).

z	A_{24}	B_{24}
0.0	0.417	1.032
0.2	0.502	1.169
0.4	0.528	1.272
0.6	0.573	1.270
0.8	0.445	1.381
1.0	0.358	1.565
1.2	0.505	1.745
1.4	0.623	1.845
1.6	0.391	1.716
1.8	0.072	1.642
2.0	0.013	1.639
2.2	0.029	1.646
2.4	0.053	1.684
2.6	0.162	1.738
2.8	0.281	1.768
3.0	0.371	1.782

Table A2. This table summarizes various range of the IR and radio luminosity ratios mean values found in the literature. A non-exhaustive list of paper is presented as per the following: reference, redshift, environment, value q_{24} , q_{FIR} , and value of q_{TIR} along with the available either a dispersion or an error of the mean.

Reference	Redshift	Environment	Mean q_{24}	Mean q_{FIR}	Mean q_{TIR}
This work	~ 0.54	Cluster	0.69 ± 0.55	1.80 ± 0.53 ; $\lambda(42-122)$	2.10 ± 0.53 ; $\lambda(8-1000)$
Reddy & Yun (2004)	$0.0120 < z < 0.025$	Cluster	–	2.07 ± 0.74 ; $\lambda(42-122)$	–
Yun et al. (2001)	≤ 0.16	Field	–	2.34 ± 0.01 ; $\lambda(42-122)$	–
Murphy et al. (2009a)	~ 0.0036	Cluster	–	2.10 ± 0.25 ; $\lambda(42-122)$	–
Rieke et al. (2009)	≤ 0.088	Field	1.22 ± 0.02	2.42 ± 0.23 ; $\lambda(42-122)$	–
Miller & Owen (2001)	$0.016 < z < 0.033$	Cluster	–	2.30 ± 0.20 ; $\lambda(42-122)$	–
Andersen & Owen (1995)	$\ll 0.2$	Cluster	–	2.27 ± 0.20 ; $\lambda(42-122)$	–
Younger et al. (2009)	$1.5 < z < 3.0$	Field	–	2.23 ± 0.04 ; $\lambda(40-120)$	–
Sajina et al. (2008)	$0.5 < z < 3.0$	Field	–	2.07 ± 0.01 ; $\lambda(40-120)$	–
Kovács et al. (2006)	$1 < z < 3$	Field	–	2.07 ± 0.09 ; $\lambda(42-122)$	–
Garrett (2002)	≤ 1.4	Field	–	2.00 ; $\lambda(40-120)$	–
Helou et al. (1985)	~ 0.0036	Field	–	2.14 ± 0.14 ; $\lambda(42-122)$	–
Bourne et al. (2011)	$0 < z < 2$	Field	1.47 ± 0.03	–	2.66 ± 0.12 ; $\lambda(8-1000)$
Sargent et al. (2010a)	$0 < z < 5$	Field	1.26 ± 0.13	–	2.57 ± 0.13 ; $\lambda(8-1000)$
Sargent et al. (2010b)	$0 < z < 2$	Field	–	–	2.585 ± 0.245 ; $\lambda(8-1000)$
Ivison et al. (2010a)	$0 < z < 3$	Field	–	–	2.41 ± 0.20 ; $\lambda(8-1000)$
Ivison et al. (2010b)	$0 < z < 2$	Field	–	–	2.40 ± 0.24 ; $\lambda(8-1000)$
Jarvis et al. (2010)	$0 < z < 0.5$	Field	–	–	2.40 ± 0.12 ; $\lambda(8-1000)$
Murphy et al. (2009b)	$0.6 \leq z \leq 2.6$	Field	–	–	2.41 ± 0.30 ; $\lambda(8-1000)$
Bell (2003)	Local	Field	–	2.36 ± 0.02 ; $\lambda(42-122)$	2.64 ± 0.02 ; $\lambda(8-1000)$
Garn et al. (2009)	$0 < z < 2$	Field	0.92 ± 0.10	–	–
Beswick et al. (2008)	$0 < z < 1.2$	Field	0.52 ± 0.20	–	–
Ibar et al. (2008)	≤ 3.5	Field	0.71 ± 0.47	–	–
Boyle et al. (2007)	≤ 2.15	Field	1.39 ± 0.02	–	–
Murphy et al. (2006)	≤ 0.002	Field	0.92 ± 0.35	2.33 ± 0.14 ; $\lambda(42-122)$	–
Appleton et al. (2004)	≤ 2	Field	0.94 ± 0.23	–	–

A1 IR Luminosities inferred from empirical relations

A1.1 Estimating total IR luminosity (L_{TIR})

Measurement of IR luminosity can be made through an empirical relation via either a single IR band or a combination of many IR bands. The total IR luminosity for our sources was solely determined through the MIPS 24 μm empirical relation.

Rieke et al. (2009) compute total IR luminosity (L_{TIR}) as described in Sanders et al. (2003) and Sanders & Mirabel (1996). The luminosity estimator of Sanders & Mirabel (1996) is defined at $\lambda = 8-1000 \mu\text{m}$; $L(\text{TIR}; 8-1000 \mu\text{m})$ and L_{TIR} is given by

$$L_{\text{TIR}} [L_{\odot}] \sim 4.93 \times 10^{-22} (13.48L_{\nu}(12 \mu\text{m}) + 5.16L_{\nu}(25 \mu\text{m}) + 2.58L_{\nu}(60 \mu\text{m}) + L_{\nu}(100 \mu\text{m})),$$

where L_{ν} [$\text{erg s}^{-1} \text{Hz}^{-1}$] is defined as the luminosity per unit frequency at a frequency $\nu = c/\lambda$, where c is the speed of light.

In this work, L_{TIR} was computed using the 24 μm luminosity ($L_{24 \mu\text{m}}$) via an empirical relation of Rieke et al. (2009, see equation A6), which is given by equation (A1)

$$\log L_{\text{TIR}} = (1.445 \pm 0.155) + (0.945 \pm 0.016) \log L_{24 \mu\text{m}}. \quad (\text{A1})$$

Furthermore, in order to be consistent throughout our calculations and comparisons, we also used other formulations of Rieke et al. (2009) to estimate the $L_{60 \mu\text{m}}$ and L_{FIR} . These transformations are presented in the next sections.

A1.2 Inferring IR luminosity at 60 μm ($L_{60\ \mu\text{m}}$)

We computed the $L_{60\ \mu\text{m}}$ using the following relation taken from Rieke et al. (2009, see equation A7), which is given by equation (A2)

$$\log(L_{\text{TIR}}) = (1.183 \pm 0.101) + (0.920 \pm 0.010) \log(L_{60\ \mu\text{m}});$$

$$\text{Hence, } \log(L_{60\ \mu\text{m}}) = \frac{\log(L_{\text{TIR}}) - 1.183}{0.920}. \quad (\text{A2})$$

A1.3 Inferring far-IR luminosity (L_{FIR})

It is common to study the relationship between the IR and radio luminosity using the classical far-IR luminosity as defined by Helou et al. (1988) at $\lambda = 42\text{--}122\ \mu\text{m}$. The far-IR luminosity

$L(\text{FIR}; 42\text{--}122\ \mu\text{m})$ estimator is given by

$$L_{\text{FIR}} [L_{\odot}] \sim 3.29 \times 10^{-22} \times (2.58L_{\nu}(60\ \mu\text{m}) + L_{\nu}(100\ \mu\text{m})),$$

where L_{ν} [$\text{erg s}^{-1} \text{Hz}^{-1}$] is defined as the luminosity per unit frequency at a frequency $\nu = c/\lambda$, where c is the speed of light.

In this work, we estimated the L_{FIR} based on the assumption that the global ratio of L_{TIR} , $L(\text{TIR}; 8\text{--}1000\ \mu\text{m})$, and L_{FIR} $L(\text{FIR}; 42\text{--}122\ \mu\text{m})$ luminosity is approximately 2 (see e.g. Bell 2003), and see also in L_{TIR} defined as $L(\text{TIR}; 3\text{--}1100\ \mu\text{m})$ (see e.g. Dale et al. 2001; Dale & Helou 2002). We have adopted the following relation as shown in equation (A3):

$$L_{\text{TIR}}/L_{\text{FIR}} \sim 2; \text{ or } L_{\text{FIR}} \sim 0.5 \times L_{\text{TIR}}. \quad (\text{A3})$$

This paper has been typeset from a $\text{\TeX}/\text{\LaTeX}$ file prepared by the author.